MNRAS 000, 1–11 (2015) Preprint 19 April 2016 Compiled using MNRAS LATEX style file v3.0

Physical Properties of Local Star-Forming Analogues to $z \sim 5$ Lyman Break Galaxies

Stephanie M. L. Greis[1]⋆, Elizabeth R. Stanway[1], Luke J. M. Davies[2] & Andrew J. Levan[1]
[1] *Department of Physics, University of Warwick, Gibbet Hill Road, Coventry, CV4 7AL, UK*
[2] *ICRAR, The University of Western Australia, 35 Stirling Highway, Crawley, WA 6009, Australia*

Accepted yyyy Month dd. Received yyyy Month dd; in original form yyyy Month dd

ABSTRACT

Intense, compact, star-forming galaxies are rare in the local Universe but ubiquitous at high redshift. We interpret the 0.1-22 μm spectral energy distributions (SED) of a sample of 180 galaxies at $0.05 < z < 0.25$ selected for extremely high surface densities of inferred star formation in the ultraviolet. By comparison with well-established stellar population synthesis models we find that our sample comprises young ($\sim$ 60 - 400 Myrs), moderate mass ($\sim 6 \times 10^9$ M$_\odot$) star-forming galaxies with little dust extinction (mean stellar continuum extinction $E_{\rm cont}(B-V) \sim 0.1$) and find star formation rates of a few tens of Solar masses per year. We use our inferred masses to determine a mean specific star formation rate for this sample of $\sim 10^{-9}$ yr^{-1}, and compare this to the specific star formation rates in distant Lyman break galaxies (LBGs), and in other low redshift populations. We conclude that our sample's characteristics overlap significantly with those of the $z \sim 5$ LBG population, making ours the first local analogue population well tuned to match those high redshift galaxies. We consider implications for the origin and evolution of early galaxies.

Key words: galaxies: evolution – galaxies: high redshift – galaxies: star formation

1 INTRODUCTION

Massive nearby galaxies, including the one we currently inhabit, started their lives as low-mass, low-metallicity star-forming galaxies in the early Universe. Many of these smaller progenitors likely passed through a phase in which they appeared as Lyman break galaxies, named after a distinctive drop in their observed flux shortwards of their rest-frame Lyman-limit at 912 Å caused by intervening clouds of neutral hydrogen. These galaxies are intensely star-forming systems, and are thought to be comparable to the population whose ultraviolet flux caused the reionization of the Universe before $z \sim 6$ (see e.g. Harford & Gnedin 2003; Rhoads et al. 2013; Bunker et al. 2010). LBGs are also primary sources for our understanding of the formation and evolution of galaxies (e.g. Stanway & Davies 2014). As well as being relatively straightforward to select in observations, they are thought to be the progenitors of ellipticals (Douglas et al. 2007) and spheroidal components of spiral galaxies (Verma et al. 2007) in the current epoch.

An estimate of the object's redshift is found by identifying the redshifted Lyman break wavelength as lying between a pair of photometric filters. Steidel et al. (1996) developed the drop-out technique using *UGR* filters, thereby favouring the discovery of $z \sim 3-4$ LBGs, which drop out in the U-band. Since then many studies have been undertaken on both $z \sim 3$ LBGs and their local analogues. Direct observations of $z \sim 3$ LBGs reveal their rest-frame optical properties (e.g. Shapley et al. 2001), luminosity functions (e.g. van der Burg et al. 2010), UV-optical SEDs (e.g. Papovich et al. 2001) and ultraviolet properties (e.g. Rafelski et al. 2009; Ly et al. 2011; Boutsia et al. 2014). Selected local galaxies, including highly ultraviolet-luminous starbursts at $z \sim 0.1-0.2$ (UVLGs, Heckman et al. 2005, 2011) and the extreme optical emission line galaxies (EELS, EELGs or 'Green Peas' Cardamone et al. 2009; Amorín et al. 2015), have been proposed as good local laboratories in which to study the physics of the $z \sim 3$ Universe. Detailed studies can be undertaken on such sources that would be challenging on the LBGs themselves (e.g. spatially-resolved measurements of the gas kinematics, Gonçalves et al. 2010).

Colour-selected LBGs have been identified to date at redshifts $1 < z < 10$, with studies of their bulk properties including Oteo et al. (2013) for $z \sim 1$, Hathi et al. (2013) and Haberzettl et al. (2012) for $z \sim 1-3$, Mosleh et al. (2012) and Finkelstein et al. (2015)for $z \sim 1-7$, Huang et al.

⋆ E-mail: s.m.l.greis@warwick.ac.uk

(2015) for lensed $z \sim 6-10$ objects, and Bouwens et al. (2015) and Ellis et al. (2013) for $z \gtrsim 9$ candidates). However, the detailed study of high redshift LBGs, particularly at $z > 5$ is complicated by their small projected size and faint apparent magnitudes, pushing current observations to their technical limits. The interpretation of LBGs can therefore be greatly improved by studying a more nearby sample of galaxies with comparable star formation properties and physical sizes which act as Lyman break analogues (LBAs).

In this paper we extend the pilot sample identified by Stanway & Davies (2014) to define an analogue population of 180 candidate objects with $0.05 < z < 0.25$. This sample selects on the two key observable differences between $z \sim 3$ and 5: ultraviolet properties and physical size. In this paper, we aim to answer the question of whether our sample of nearby UV-selected galaxies is indeed analogous to high redshift ($z \sim 5$) LBGs and to determined the specific star formation rates and galaxy construction timescales for these sources. To answer these questions, we undertake spectral energy distribution (SED) fitting of the far-UV to near-infrared magnitudes of the objects, and determine their masses, star-formation rates (SFRs), metallicities, dust contents, and ages.

In section 2 of this paper we present the LBA candidates sample, selected from SDSS DR7 and GALEX DR6, and supplemented with spectroscopic data from the enhanced catalogue provided by the MPA-JHU collaboration. The wavelength coverage is extended to the infrared (using WISE and 2MASS data) in section 3. In section 4 we give an overview of the SED fitting procedure and stellar population spectral synthesis codes used to determine the galaxies' properties. We present the results of the SED fitting in section 5, before presenting the inferred properties of our sample in 6. In section 7 we determine the suitability of our sample as analogues to $z \sim 5$ galaxies. We present our conclusions in section 8.

Throughout this paper, magnitudes are given in the AB system. We adopt a standard ΛCDM cosmology with $H_0 = 70\,\mathrm{km\,s^{-1}\,Mpc^{-1}}$, $\Omega_M = 0.3$ and $\Omega_\Lambda = 0.7$.

2 SAMPLE SELECTION

2.1 Previous Work

While analogue samples for $z \sim 3$ Lyman break galaxies have been established by Heckman et al. (2005) and Hoopes et al. (2007), Stanway & Davies (2014) argue that they are an unsuitable analogue populations for higher redshift ($z \sim 5$) LBGs, as the redshift evolution of Lyman break galaxies must be taken into account when determining the appropriate selection criteria for their local analogues.

LBGs at $z \sim 5$ are less luminous (see Bouwens et al. (2007)), younger and less massive (see Verma et al. (2007), Oesch et al. (2013)), and have lower metallicities (Douglas et al. 2010) than $z \sim 3$ LBGs. The star formation rate density within LBGs increases by a factor of $\sim 4-5$ from $z \sim 5$ to $z \sim 3$ (van der Burg et al. 2010). They are also significantly more compact than their $z \sim 3$ counterparts (Wilkins et al. 2011; Mosleh et al. 2012), which has implications for the physical processes within the galaxies. The compactness modifies star formation since a higher UV-photon density causes higher dust and intergalactic medium temperatures, than would be present in more distributed star-forming regions, which thus affects the collapse of molecular clouds into stars, the ionization of the intergalactic medium and potentially the mode of star formation itself (see e.g. Stanway et al. 2014). By comparing the star formation densities of the Hoopes et al. (2007) sample with those of typical values for LBGs at higher redshifts, Stanway & Davies (2014) indicate that only $\sim 3\%$ of the Hoopes et al. (2007) sample of UVLGs have a star formation density comparable to that observed in distant LBGs. This discrepancy only becomes exacerbated as the Lyman break samples are pushed to higher redshifts.

In order to establish our sample, we modify the pilot sample established by Stanway & Davies (2014). which was constrained to declinations of $< -8^o$ to facilitate follow-up from Southern telescopes. We lift this constraint, considering the full SDSS-GALEX overlap region.

2.2 UV and Optical Selection

Potential candidates are identified from data release six (DR6) of the publicly available *GALEX* survey[1] (Martin et al. 2005) and DR7 of the Sloan Digital Sky Survey (SDSS, Abazajian et al. 2009), providing ultraviolet and optical data respectively. Candidates are selected such that their UV colours satisfy $-0.5 < FUV - NUV < 0.5$ or $-0.5 < FUV - r < 1.0$, where FUV and NUV correspond to the observed frame *GALEX* far- and near-ultraviolet bands at ~ 1500Å and ~ 2300Å respectively, while r indicates the *SDSS* red band at ~ 6200Å. We set this restriction to ensure that the rest-frame UV slope is close to flat, indicative of a recently formed population of young stars with ages < 200Myrs.

In addition to colour constraints, the luminosities of the potential analogue galaxies are matched to those of high redshift LBGs. Bouwens et al. (2007) find that the absolute magnitude of galaxies becomes 0.7 mag brighter between $z \sim 7$ and $z \sim 4$, primarily due to the hierarchical coalescence and merging of galaxies; we thus select candidate galaxies such that their FUV absolute magnitudes are equivalent to those of the existing $z > 5$ LBG populations, by requiring that $L_{UV} = 0.1 - 5L^{\star}_{z=6}$ where $M^{\star}_{UV} = -20.24$ at $z \sim 6$ (Bouwens et al. 2007). Neither the luminosities of the high redshift population nor those of this analogue sample is corrected for dust extinction, as we discuss later. In order to select comparable star formation densities to the high redshift LBG population, candidates should have a projected half-light radius < 2kpc. This is not always possible to determine reliably in ground-based SDSS imaging. We allow for unresolved sources, so that objects are selected which subtend $< 1.2''$ or $r_{1/2} < 3.5\,\mathrm{kpc}$ in the galaxy's rest-frame where this can be measured (see Stanway & Davies 2014). It should be noted that these constraints are applied using optical (g and r bands) rather than ultraviolet images as available *GALEX* images do not offer sufficient resolution.

We require the candidates to have SDSS spectroscopy, which both identifies the precise redshift of the galaxies and confirms the source of their UV luminosity as most likely

[1] http://galex.stsci.edu/GR6/

Figure 1. Distribution over redshift z of the sample of 180 candidate galaxies. The median redshift of ∼0.14 is indicated by the dashed vertical line.

arising from star formation instead of active galactic nucleus (AGN) activity. We exclude galaxies with an AGN component identified by the SDSS spectroscopic pipeline, since AGN are known to be rare in the distant galaxy population; see Douglas et al. (2007) for $z \sim 5$ or Nandra et al. (2005) for $z \sim 3$ observations. Additionally, we perform an initial, by eye, assessment of the reliability of these sources to exclude sources with clearly inaccurate photometry or multicomponent sources in which only a small region satisfies our criteria. All galaxies in the sample have very low mean Galactic foreground reddening (Schlafly & Finkbeiner 2011) ranging between $0.007 \leqslant E(B-V)_{SFD} \leqslant 0.088$, with a mean extinction of 0.025. We adjust their photometry for this using the Milky Way extinction law of Allen (1976).

The redshift distribution of our resulting sample of 180 candidate galaxies at $0.05 < z < 0.25$ is shown in Fig. 1.

3 INFRARED PHOTOMETRY

We determine photometry for the sample from the Widefield Infrared Space Explorer (WISE, Wright et al. 2010) and 2-Micron All Sky Survey (2MASS, Skrutskie et al. 2006) images, such that we have photometric data spanning a combined wavelength range of approximately 1500 Å to 22μm. For consistency we determine either measurements or limits on the galaxies' magnitudes from the infrared imaging using fixed aperture photometry at the SDSS locations and the recommended aperture sizes appropriate to point sources. The sources were selected to have no nearby neighbours in the optical or ultraviolet, and so did not require model-dependent deblending. However in 10% of the sample 2MASS photometry at the source location was unreliable due to high local noise or close and blended neighbours. Approximately a third of the candidate objects are individually undetected above a 2σ detection limit in one or more infrared bands, where this limit is determined locally in each band.

4 SED FITTING

A galaxy's spectral energy distribution can, in principle, provide detailed information about its properties, including stellar mass, star formation rate, metallicity, and dust content. The flux in different wavebands is compared to synthetic spectra created from a library of either empirical or stellar population synthesis (SPS) model templates. These models comprise the integrated spectra of artificial stellar populations, the shape and magnitude of which depend on the star formation history, metallicity and initial mass function (IMF), which themselves shape distributions in stellar age and mass. As a result, the choice of SPS model can affect the derived parameters. Here we compare results using the Maraston (M05, 2005) SPS models against templates created using the Binary Population and Spectral Synthesis SPS code (BPASS, Eldridge & Stanway 2009, 2012).

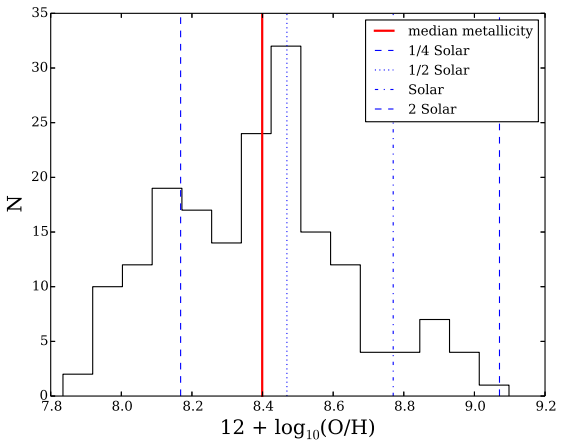

Figure 2. The oxygen abundance distribution of our sample as calibrated from strong emission line ratios in SDSS spectroscopy, using the line diagnostic of Dopita et al. (2016). Dashed vertical lines indicate 0.25, 0.5, 1 and 2 times the local Galactic concordance value of 12+log(O/H)=8.77 which has been proposed as a better calibration than bulk Solar abundance. Solid vertical line indicates the sample median.

Maraston models: As described in Maraston (2005), the Maraston models generate composite stellar populations (CSP) with a Salpeter IMF and star formation rates which decline exponentially with time such that, $\dot{M} \propto e^{-t/\tau}$, where τ is the e-folding timescale. These are built by combining simple single-age stellar population models which have been calibrated against globular cluster data for which ages and element abundances are independently known, so that various generations of stars can be modelled (Maraston 2005). The parameters of the physical inputs in the models, such as convection, mass loss, and mixing, which could not be derived from first principles, are thus fixed by observations.

For our SED fitting procedure, we allowed timescales τ, of 100 Myr, 500 Myr and 1 Gyr. We constrain the metallicity of our input models to 0.5 Solar which is a good match for the metallicity derived from nebular emission in these sources, as derived from the calibration of Dopita et al. (2016) and shown in Fig. 2.

BPASS models: The Binary Population and Spectral Synthesis code, or BPASS[2], was developed to address the effects of massive star evolution on the SED of galaxies (Eldridge & Stanway 2009, 2012, Eldridge et al in prep). While in young stellar populations a galaxy's spectrum is dominated by the radiation emitted by massive hot stars, a more aged population shows a spectrum which is strongly influenced by the evolution of moderately massive stars that live for longer than the most massive population. This evolution is often modified by processes such as angular momentum transfer, and mass loss and gain due to a binary companion, allowing evolved secondary stars to extend their highly luminous phase, and to boost the population of rapidly rotating H-depleted Wolf-Rayet stars (Stanway et al. 2014).

[2] See http://bpass.auckland.ac.nz

The standard BPASS distribution provides model spectra for instantaneous starbursts. From these, we construct exponentially declining star formation history models, to match those available in the Maraston models.

We use v2.0 of BPASS (Eldridge et al. in prep) and again select the $0.5\,Z_{\odot}$ models and an initial mass function with a typical Salpeter slope of -2.35 for stars between 0.5 and $100M_{\odot}$, and a slope of -1.3 for stellar masses between 0.1 and $0.5M_{\odot}$.

The stellar flux output in the BPASS model is processed to estimate the nebular emission component using the radiative transfer code CLOUDY (Ferland et al. 1998). We select an electron density of $10^2\,\mathrm{cm}^{-3}$, a covering fraction of 1, and a spherically symmetric gas distribution with inner radius of 1 pc. These are appropriate for a H II region, as discussed in Eldridge & Stanway (2012) and Stanway et al. (2014).

Dust modelling: The template spectra are modified using the Calzetti et al. (2000) dust extinction law, which was empirically derived for local infrared-luminous galaxies with active star formation. In the Calzetti law the extinction in front of nebular line emission regions is higher than that on the stellar continuum such that $E_{\mathrm{cont}}(B-V) = 0.44 \times E_{\mathrm{line}}(B-V)$. For broadband photometry, the emission is dominated by stellar continuum.

At each model age, we modify the synthetic SED by a reddening curve corresponding to colour excesses in the continuum, $E_{\mathrm{cont}}(B-V)$, between 0.0 and 0.6 mags (in steps of 0.05). We do not constrain the dust using the observed nebular emission since it is likely that the nebular emission regions are significantly smaller than the galaxy as a whole (Finkelstein et al. 2009; Scarlata et al. 2009), and so the dust measured by the Balmer decrement may well not be representative of the stellar continuum emission.

Fitting Procedure: A typical source in our sample is well detected in the optical and ultraviolet, but often weakly detected or undetected in the near-infrared. Their mid-infrared (WISE) properties vary significantly. Given the number of parameters required both to build a stellar population, and to be inferred from the resulting template, any SED-fitting procedure can be subject to substantial uncertainty and degenerate solutions. The number of extracted parameters can be comparable to the number of input data-points.

Given that the relatively new BPASS models are not integrated into most existing fitting codes, and in order to retain physical insight into the input parameters, we construct our own SED fitting code. This makes use of the well-established χ^2 statistic, which is appropriate for assessing goodness of fit in samples dominated by Poisson noise, and for which the range of χ^2 values representing a $1\,\sigma$ uncertainty band on any given parameter is determined by a distribution dependent on the number of free parameters. The uncertainty range quoted on numerical values is the range of models considered with a χ^2 value with a 68 per cent or better probability of being consistent with the best fit model. We note that an alternative would involve marginalising over the Bayesian priors for this sample, however since the priors are poorly constrained, and the data is sparse, this is unlikely to produce a stronger or more reliable constraint in this circumstance.

We apply this method to fit the observational data over the spectral range 0.12-2.16 μm, i.e. from *GALEX* FUV to 2MASS K_S band inclusive. Where sources are undetected at the $2\,\sigma$ level in a given band, we use the $1\,\sigma$ flux in that band, and assign an uncertainty equal to the flux. We note that at wavelengths longwards of K_S the effects of dust extinction are negligible and thus excluding the relatively shallow WISE bands does not impact the inferred extinction. Similarly, the reprocessing of extincted ultraviolet emission by thermal dust does not produce emission shortwards of 3 microns and so no dust emission component is required for modelling the stellar population. We thus exclude the *WISE* bands from the fitting procedure since these are most strongly dependent on the dust properties adopted rather than the input stellar spectra. However we evaluate the consistency of the *WISE* data with our best fit model spectra in section 6.4.

In order to evaluate the effectiveness and reliability of our spectral fit we also make comparisons to two additional fitting methods. We make use of the enhanced spectroscopic catalogue publicly available from the MPA-JHU collaboration[3] (Brinchmann et al. 2004), containing SDSS photometric and spectroscopic data as well as inferred physical properties. These were derived from a narrower wavelength range than we consider, but make additional use of spectroscopic constraints. We find that a small number (3) of our objects are not included in the MPA-JHU catalogues, but this has no significant effect on the comparisons presented in later sections. We also consider a parallel analysis using the Maraston models and the CIGALE fitting algorithm (Burgarella, Buat, & Iglesias-Páramo 2005; Roehlly et al. 2014). This incorporates stellar, nebular, and dust extinction components which we select to range over the same values as our code. It also includes dust emission and performs a marginalisation analysis to determine the best fit. Configuring the CIGALE dust emission component requires three additional parameters and thus the number of constrained inputs is comparable to the number of photometric data points on a typical source. Nonetheless, throughout we confirm that this method produces very similar results to those of our independent fitting code. We also calculate fits extended either to the K_S band (as is the case in our own fitting) or to $22\,\mu$m band. We confirm that there is no significant difference in the observed stellar and dust extinction components if the WISE bands are included in the fit, although several additional parameters are required to do this.

5 SED PROPERTIES OF OUR SAMPLE

5.1 Masses

The best-fitting mass is one of the most robust outputs of an SED fitting procedure since it depends primarily on the optical/NIR normalisation of the spectrum (i.e. the galaxy luminosity at its known redshift) rather than the details of the spectral shape. However, there is modest dependence on the synthetic stellar population input, both in terms of that

[3] based on DR7, http://www.mpa-garching.mpg.de/SDSS/DR7/

Figure 3. The distribution of derived stellar masses, comparing the M05 and BPASS models. The median fitted values are indicated by vertical dashed lines, as are those independently found by MPA-JHU and by fitting the data with the CIGALE code and M05 models. These all show good agreement. Representative uncertainties on individual masses are indicated by points and associated ranges. The uncertainty on the median is substantially smaller.

Figure 4. Distribution of the stellar population ages of the target galaxies found using SED fitting with the M05 and BPASS models. Indicative uncertainty ranges on individual galaxies are indicated by points.

initial normalisation and since the mass to light ratio at any given wavelength depends on the stellar population.

The median stellar masses, M_*, of our sample were consistent between input templates, and found to be $\log(M_*/M_\odot) = 9.80 \pm 0.42$ for the standard BPASS model and $\log(M_*/M_\odot) = 9.31 \pm 0.34$ for the M05 model. In figure 3 we compare the distributions of masses. As expected, the derived distributions are broadly similar between different input SPS models, with no catastrophic disagreements between them. The BPASS model produces slightly higher masses than the equivalent M05 model.

The independent galaxy template fitting procedure performed for star-forming galaxies by the MPA-JHU collaboration (Brinchmann et al. 2004) shows good agreement with the SED model fits for our objects, as does a parallel fitting procedure using the M05 models and CIGALE. In the following sections, we select the BPASS model results for further analysis given the more physically motivated stellar population synthesis incorporated in these, and the generally weak dependence on input model in best-fit mass.

5.2 Ages

For most galaxies the age of the stellar population in an SED is most strongly constrained by the strength of the spectral break at around 4000Å in the rest-frame. Our selection criteria required the break to be modest, with near-flat ultraviolet to optical colours, selecting young starbursts. The population as a whole shows a relatively narrow distribution of best fit ages as figure 4 illustrates. The uncertainty on individual galaxies (i.e. the range yielding a χ^2 statistic with a probability within 68 per cent of the best fit) is somewhat larger and typical values are indicated on the figure.

The ages found using the M05 models were lower than the ones found from the BPASS models, with median ages of $\log(\text{age/yr}) = 7.78 \pm 0.49$ and $\log(\text{age/yr}) = 8.60 \pm 0.52$ respectively. The higher age found using BPASS τ models is consistent with the more massive stellar populations found in section 5.1.

5.3 Dust Extinction

In addition to the foreground extinction arising from line of sight through the Milky Way, we also fit for an internal dust extinction component for each object, applied in the objects' rest-frame. The best-fitting $E_{\rm cont}(B-V)$ values are in close agreement regardless of SPS templates adopted, giving mean

Figure 5. The distribution of $E_{\rm cont}(B-V)$ values obtained from model SED fitting (blue for BPASS, red for M05), and those calculated from the observed H_α/H_β flux ratios (assuming case B recombination with a temperature of 10^4 K and an electron density of $n_e = 10^2$ cm^{-3}, multiplied by 0.44 to recover equivalent continuum extinction; black).

Figure 6. BPT diagram for our sample, with colour coding according to the masses determined by SED fitting. The blue dot-dashed line indicates the average value for local galaxies (Steidel et al. 2014), while the red dotted line shows the average of redshift $z \sim 2$ star-forming galaxies (Steidel et al. 2014). The solid black line indicates the proposed maximal starburst (Kewley et al. 2001), and the black dashed line shows the standard criterion used to separate AGN from star-forming activity (Kauffmann et al. 2003). Only a few targets fall above the dashed line, indicating that they might include an AGN component.

$E_{\rm cont}(B-V)$ values of 0.16±0.10 for the M05 templates and 0.12±0.07 for the BPASS models, as shown in figure 5.

We also calculate an estimate of dust extinction from the ratio of recombination line strengths in the objects' spectra. For this we assume an intrinsic Balmer decrement for case B recombination, at a temperature of 10^4 K and an electron density of $n_e = 10^2$ cm^{-3}, such that H_α/H_β=2.86. For comparison with the stellar continuum derived extinctions, we adjust this $E_{\rm line}(B-V)$ value by a factor of 0.44. As figure 5 shows, the resultant $E_{\rm cont}(B-V)$ value distribution shows good agreement with those calculated from model SED fits.

6 INFERRED PROPERTIES

6.1 Excitation Measurements

The BPT diagram (Baldwin et al. 1981) indicates the origin of the ionizing radiation heating the nebular gas in a galaxy on the basis of its [O III], Hβ, [N II] and Hα flux ratios. This allows the classification of the ionizing spectrum into star-forming or AGN-driven. Using the BPT diagram as a diagnostic for our sample (Fig. 6) we determine that the majority of sources fall below the proposed cut-off separating star formation and AGN activity (black dashed line, Kauffmann et al. 2003), thus confirming that these are indeed star-forming galaxies and verifying the effectiveness of the SDSS spectroscopic analysis pipeline. Four objects fall into the 'composite' region, indicating that these sources may contain components of both star formation and AGN activity. While it is noteworthy that our sample typically lies well above the median relation seen in local galaxies, none of the objects in our sample lie above the limit determined by Kewley et al. (2001) for a 'maximal' starburst.

The mass-excitation (MEx) diagnostic developed by Juneau et al. (2011) provides an alternative indication of the AGN contribution within a galaxy, similar to the BPT diagnostic but with the separation between star-forming galaxies and AGN-hosts enhanced by the effects of the mass-metallicity relation for local sources. Fig. 7 shows the [O III]/Hβ vs mass plane for the objects in our sample. Again, the majority of our objects trace the starburst galaxy region of the parameter space, but, even more so than in the

Figure 7. Mass-excitation diagram for our sample (red crosses) and SDSS galaxies (underlying grey distribution). The galaxies in our sample appear to be irradiated by a significantly higher ionizing potential than other local galaxies of comparable mass. The dashed lines indicate proposed classifications between AGN (above line), composite (bordered region), and star formation activity (below line) according to Juneau et al. As in the BPT diagram, the majority of our objects are found in the star-forming region.

Figure 8. The median, upper and lower quartile dust-corrected star formation rates (SFRs) of the sample. All fluxes were corrected for Milky Way dust attenuation. The [O II]and Hα fluxes were further corrected for the object-intrinsic dust extinction with $E_{\rm line}(B-V)$ values found using the (Milky Way dust-corrected) Balmer decrement, and the U-band and UV corrected using $E_{\rm cont}(B-V)$ determined by SED fitting. The UV SFR found without applying an intrinsic dust correction is shown underneath the corrected value. We show two calibrations for the W4 band - that of Cluver et al. (2014) as (a) and Lee et al. (2013) as (b). The SFRs determined by MPA-JHU are shown as a comparison. Sample medians derived using the CIGALE parameter marginalisation code and the M05 stellar models, averaged over two different timescales, are indicated by vertical lines.

BPT diagram, we see an offset between our population and the local SDSS sample from which it was drawn, pushing our sample to straddle the border of AGN classification. Such a shift is likely indicative of a harder ionizing flux, and associated higher ionization potential but not necessarily one arising from AGN (see Stanway et al. 2014). This may indicate a difference in the galaxy mass-metallicity relation between our sample and more typical galaxy populations at the same redshift, with relatively little dependence of metallicity on mass for these intense starbursts.

6.2 SFRs

In our SED fitting analysis we allowed star formation rate to vary as this was constrained by the combination of SFR timescale, mass, extinction and stellar population age. We note that while it might have been possible to pre-constrain this using nebular line emission, such constraints would have been dependent on dust extinction, and star formation history assumed in the calibration used. To explore the effect of such assumptions, and their appropriateness for this sample, we determine the SFRs of our galaxies using a range of established SFR indicators, from UV to mid-infrared wavelengths.

UV: We calculate SFRs from dust-corrected FUV fluxes using the Madau et al. (1998) prescription at 1500 Å for a Salpeter IMF. For a stellar population with ongoing continuous star formation dominated by young stars, the UV luminosity is a good tracer of the stellar birth rate and independent of the star formation history if the age $t \gg t_{MS}$, where $t_{MS} \leqslant 2\times10^7$ yrs for late-O/early-B type stars (Madau et al. 1998). For comparison, we also calculate SFRs based on the SDSS u-band photometry, after correcting for dust, using the calibration of Hopkins et al. (2003) - as figure 8 shows, this is associated with a relatively large uncertainty, but is comparable to the dust-corrected FUV-derived SFR.

Hα and [O II]: We calculate the SFRs from Hα and [O II] fluxes, using standard conversion factors (Kewley et al. (2004), see also Kennicutt (1998)). The SDSS fibre [O II] and Hα fluxes are not corrected for fibre losses since our targets are very compact, but are corrected for nebular dust extinction as described above. Both strong line indicators are very sensitive to instantaneous star formation, i.e. stellar ages $< 3-10$ Myr, but also sensitive to the ionization conditions and metallicity of the nebular gas and so the applicability of these calibrations in this sample has not been verified. The UV and the spectral line indicators agree within a factor of a few, and it can thus reasonably be assumed that the galaxies are experiencing an ongoing starburst on timescales of at least a few tens of Myr.

W3 and W4: The SFRs inferred from the infrared bands were found using the empirical Lee et al. (2013) prescription for WISE bands W3 and W4. These SFR indicators were calibrated for a large sample of local star-forming galaxies with SFR > 3 M$_\odot$ yr^{-1} and mid-infrared data. Galaxies with apparent AGN activity were excluded from the calibration. For W4, we also use the calibration of Cluver et al. (2014), which is based on the local Galaxy and Mass Assembly (GAMA) survey (Liske et al. 2015; Driver et al. 2011). The median SFRs we obtain from W3 and W4 are 4.9 and 2.4 M$_\odot$ yr^{-1} respectively (based on the Lee et al calibration). As mentioned in section 6.4, the PAH emission region falls into the W3 and W4 bands, and can dominate the infrared luminosity of star-forming galaxies and hence this empirical calibration is somewhat redshift-dependent. In addition, the emission from thermal dust components has a relatively long timescale (>100 Myr) to become established after the onset of intense star formation and does not always trace the youngest starbursts (Davies et al. 2015). We note that some of the W3 and W4 magnitudes in our sample were upper limits, these have been included in this median with a nominal SFRs equal to the 1σ flux limits. As a result, the derived median values may be skewed by these inferred limits on SFR.

The median, upper and lower quartile SFRs derived for the entire sample are shown in Fig. 8. The different SFR indicators, as well as the independently determined MPA-JHU results, are in good agreement, with the median values of each indicator lying between ~ 2.5 and 14 M$_\odot$ yr^{-1}, albeit with large ranges. The highest SFRs are found from the dust-corrected UV fluxes, but are associated with considerable uncertainty on the dust extinction correction. We also show UV SFRs without correction as they provide a lower limit on the SFR in the objects. An additional constraint on SFR can be obtained from the SED fitting procedure, although this depends on the star-forming population dominating the stellar light. The star formation rates derived from our BPASS models are comparable to the rest-UV estimates with a median of $\sim$15 M$_\odot$ yr^{-1}. Those derived from the M05 models (either using our fitting procedure or CIGALE) are slightly lower with a median around $\sim$8 M$_\odot$ yr^{-1}. Interestingly, in both cases, the average SFR over 100 Myr timescales is higher than the instantaneous SFR, suggesting that this is decreasing over time for the median galaxy. Our sample's best-fitting ages (as described in section 5.2) of a few tens to a few hundreds Myrs, and the uncertain contribution of strong line emission to the WISE bands, suggest that the Hα and UV SFR indicators are most likely to provide accurate descriptions of the objects, sub-

Figure 9. Specific star formation rate (as $\log_{10}(\mathrm{sSFR/Gyr^{-1}})$) vs mass of our sample (red dots), using the Hα SFR conversion. The green dashed and dot-dashed lines represent constant star formation rates of 10 $M_\odot$ yr^{-1} and 1 $M_\odot$ yr^{-1} respectively. The red lines represent the star formation main sequence at different redshifts according to Leslie et al. (2016). The underlying grey distribution gives the logarithm of the local SDSS galaxies' distribution. It is apparent that our objects lie significantly above the main sequence for local galaxies.

Figure 10. The distribution of the inverse specific star formation rate. This corresponds to the mass doubling time scale of the galaxies. The median value of 1.0 Gyr is shown by the vertical red dotted line.

ject to uncertainties in extinction and differences in emission timescale.

6.3 Specific Star Formation Rates and Timescales

From the star formation rates calculated from Hα in section 6.2 and the masses derived in section 5.1, we calculate the specific star formation rates (sSFR = SFR/mass) and star formation rate surface densities (Σ_{SFR} = SFR/area). The galaxies in our samples have $\log(\mathrm{sSFR/yr^{-1}}) \sim -9.00 \pm 0.47$. As shown in Fig. 9, these sSFRs indicate that our sample is more intensely star-forming at a given stellar mass than more typical local galaxies. Our galaxies lie significantly above the star-forming galaxy main-sequence for $z \sim 0$. While our galaxies show a mild evolution in sSFR with mass (consistent with our ultraviolet luminosity, and hence SFR, selection criteria), we do not find any correlation of sSFR with redshift over the narrow redshift range spanned by the sample.

The inverse of the specific star formation rate, sSFR^{-1}, provides a measure of the time it would take to double the stellar mass of the system assuming constant star formation at the present rate. In order to calculate this mass doubling time scale, we use the star formation rates derived from Hα. We find that the mass doubling time scales of our sample have a median of 1.0 Gyr as shown in Fig. 10.

6.4 Dust Emission

Our fit to the optical to near-infrared data is not sensitive to the reprocessing of ultraviolet emission in the thermal infrared. However, the observed extinction and inferred stellar continuum can be used to predict the expected emission if there is no additional, heavily-obscured star-forming or AGN component. To model the re-emission of thermal photons at long wavelengths, we adopt the energy-balance prescription of da Cunha et al. (2008). While this is implemented in the MAGPHYS code, it represents a simple formulation in which the energy lost from UV-optical is re-emitted as a combination of grey-body and polycyclic aromatic hydrocarbons (PAH) emission components. We reproduce this in our own SED fitting code, using identical black body parameters to those derived by da Cunha et al. (2008) as the MAGPHYS defaults for star-forming galaxies. We do not attempt to vary these parameters or fit the shape of the dust emission curve, since two data points, with typical signal to noise < 10 on each, is insufficient to do so. Instead, we simply consider constraints on normalisation for a single possible emission spectrum. For the PAH emission component, we used the average luminosity-weighted composite template of Smith et al. (2007), which is based on low resolution mid-infrared *Spitzer Space Telescope* spectroscopy for nearby AGN and star-forming galaxies. The luminosity of intensely star-forming galaxies in the mid-infrared ($\sim 3-25$ μm) is dominated by strong emission features attributed to PAHs, with up to 20% of the infrared flux emitted in the strong transition lines alone.

Comparing the measured infrared fluxes (or upper limits) with our best-fitting model SEDs, we find no significant discrepancy between these in the near-infrared shortwards of the K_S band. However, in the PAH-dominated region of $\sim 3-25\mu$m, we see an offset between model and observation. Figures 11 and 12 show this offset for the WISE W3 and W4 bands centred at 12 and 22 μm respectively. At 12 μm (observed) the models marginally under-predict the galaxy flux, based on our fitted extinction and assumed dust emission law. No significant difference in behaviour is observed between the M05 and BPASS models.

In the W4 band, however, predicted magnitudes derived from the BPASS model are in much better agreement with the observed values than those found using the M05 model. This suggests that, given the combination of BPASS stellar models and Calzetti et al. dust extinction, the Smith et al. composite luminosity-weighted average spectrum provides a reasonable estimate of the PAH component. However, if the M05 stellar population synthesis model better describes the population, a steeper PAH model with increased flux at higher wavelengths (see Fig. 18 in Smith et al. 2007) may be more appropriate.

An extinction law which absorbs more flux at short wavelengths would also lead to stronger IR dust emission and hence stronger PAH features. Our use of the Calzetti law was motivated by its description of intensely star-forming systems - exceeding the star formation rate of the Milky Way or other sites, for which dust law formulations exist, and more akin to the galaxies in our sample. While it was originally developed for a small sample of UV and FIR-bright galaxies, Calzetti et al. also confirmed the applicability of the dust reddening law on a larger sample of starburst galaxies, and it is widely used for starbursts across a broad redshift range.

The thermal dust emission is modelled here as a series of single temperature grey-bodies. A change in the dust grain size or composition may modify these. We note that fitting using the CIGALE code, which scales a dust emission curve derived from Dale et al. (2014), but otherwise has identical input stellar populations to ours, overpredicts the median model flux by 40 per cent. However, in deriving this, we had to assume three default dust parameters to fit data essentially constrained by two points. We would suggest that further investigation of the mid-infrared properties of this or similar samples may be required.

Figure 11. Comparing the observed WISE 3 magnitude to the colour difference between the SED model and observations. The red dots indicate the M05 model results, while the BPASS model results are represented by blue crosses. The dashed line marks the magnitude line where model and observations coincide. For WISE 3, at 12μm, no significant difference can be seen between the two models.

Figure 12. Same as Fig. 11 but for the WISE 4 band at 22μm. Both model sets underpredict mid-infrared emission. A clear offset between the M05 and BPASS model can be seen with the BPASS (blue crosses) model's magnitudes in better agreement to the observed ones.

Figure 13. The specific star formation rate (sSFR) of our sample (red squares) compared to other galaxy populations at different redshifts. We split our sample into two redshift subsets, at $0.05 < z < 0.15$ and $0.15 < z < 0.25$, and indicate the mean of the entire sample with a dotted line. The average sSFR of our sample is significantly higher than that of other local and low-redshift galaxies, but in very good agreement with the sSFRs found for $4 < z < 6$ LBGs.

7 SUITABILITY AS LYMAN BREAK ANALOGUES

7.1 Implications for $z \sim$5 LBGs

Our sample was selected for their potential use as analogues to the most distant galaxy populations. In table 1 we summarise the inferred physical properties of our sample, and also those derived for the high redshift galaxy population. In many respects these are similar, with comparable dust extinction, stellar mass, stellar age, metallicities, star formation rates and sSFRs.

A small number of our larger, older galaxies may be inappropriate as analogues for the distant galaxy population. None of the objects in our sample have masses greater than 5×10^{10} M$_\odot$, and 132/180 objects satisfy a mass criterion of M$< 10^{10}$M$_\odot$. Further excluding all objects with ages greater than one Gyr leaves 124/180 sources, while only accepting those with ages $< 10^{8.5}$ years, produces a young subsample of 78/180 galaxies (none of which show AGN features).

In Fig. 13 we consider the specific star formation rate of our sample in comparison to more typical galaxy populations as a function of redshift. We make use of the high signal to noise Hα measurement for SFR, and apply a conservative correction, increasing the SFR by 25 per cent to account for the more mature star formation component which would be measured in the ultraviolet. We note that our UV-derived star formation measures are larger than this corrected value, but associated with large uncertainties on dust extinction. Thus we consider the values in the figure as realistic lower limits on the sSFR. At low redshifts our sample is very atypical of the bulk of the population. At high redshifts, LBGs constitute the majority of the observable galaxy sample. It is apparent that the sSFRs of our sample lie significantly above those for more typical local galaxies (measured in Hα). In this respect they are more akin to those seen in $z \sim 4-6$ LBGs (as can also be seen in Fig. 9), which are also an extreme, ultraviolet-selected star-forming population. The high sSFRs in this sample also provide a possible explanation for the high excitation parameters seen in them (see Fig. 7) and poses interesting questions. These include their escape fraction of ionizing radiation, and its comparison to those inferred in high redshift galaxies?

Figure 14. The absolute (dust-corrected) 1500 Å *FUV* magnitude vs mass distribution of our sample. The black solid line shows the theoretical prediction for $z \sim 5$ galaxies by Dayal et al. (2014); lines for $z \sim 7$ and 9 are also shown on the plot. The blue circles give the mean values of our sample, binned in 0.5 dex mass increments, and their standard errors. The M$_{UV}$ uncertainties are too small to be seen. The red error bars are indicative of the uncertainty on each individual datum contributing to a given bin. For comparison, the distribution for galaxies measured by the GAMA survey (Liske et al. 2015) at the same redshift as our sample is shown in grey.

We calculate the ultraviolet continuum mass to light ratio for our sources, using masses determined via SED fitting and dust-corrected 1500 Å *FUV* fluxes as shown in Fig. 14. We compare this to the theoretical predictions of Dayal et al. (2014, dashed black line) for $z \sim 5$ galaxies, and also with the ultraviolet luminosities of more typical low redshift star-forming galaxies selected from the GAMA survey (Liske et al. 2015, greyscale). For the latter, we apply the Calzetti law and the extinction reported by the GAMA team to correct for dust extinction. The Dayal models apply a prescription for supernova-driven wind quenching of star formation based on a semi-empirical galaxy evolution model. Our sources are offset from the local GAMA sample, but in very good agreement for the predicted $z \sim 5-9$ population, suggesting that the properties of this sample may be driven by the same evolutionary pressures and feedback constraints that apply in the distant Universe.

If the galaxies comprising our sample were redshifted to $z \sim 5$, corresponding to an age of the Universe of ~ 1.15 Gyr, their mean mass doubling time scale would place their formation redshift at $z \sim 22$. However, this assumes constant star formation over 1 Gyr, which would seem unlikely. The median age of the dominant stellar populations as derived from fitting M05 models would indicate that they formed as late as $z \sim 5.2$, while the BPASS model would place their formation redshift at $z \sim 7$ (based on the population averages). The latter is in very good agreement with the formation redshifts inferred for $z \sim 5$ LBGs, which Lehnert et al. (2007) found to be $z \sim 6-7$.

7.2 Comparison to Other Galaxy Populations

A number of galaxy populations have now been proposed as local analogues to high redshift LBGs. While these share a common property - the presence of intense star formation - they vary significantly in their selection criteria and observed properties. In Table 1 we also contrast our sample with some of the other suggested local analogue populations.

The most widely-used analogue sample is a selection of local ($z < 0.3$) UV-luminous ($L_{FUV} > 2 \times 10^{10} L_\odot$) galaxies (UVLGs) chosen to overlap the luminosity range of $z \sim 3$ LBGs (Heckman et al. 2005). The selection criteria for the original Heckman et al. (2005) sample and ours are very similar. They aim to reproduce the properties of similar galaxy populations, albeit populations at different epochs in the evolution of the Universe. As a result the galaxies

presented in Heckman et al. (2005), Hoopes et al. (2007), and Gonçalves et al. (2010) are significantly more massive than our sample, reflecting the evolution of mass and luminosity between $z \sim 5$ and $z \sim 3$ LBGs (see e.g. Verma et al. 2007). We find that only one of our 180 objects overlaps with the Hoopes et al. (2007) sample.

Similarly, blue compact dwarfs (BCDs, Zwicky 1965) are characterised by compact and gas-rich regions of high star formation. However, unlike our sample, BCDs are representative of the extremely low end of galaxy luminosity ($M_B = -18$ mag), mass, and metallicity functions. They are among the most metal-poor galaxies in the local Universe, with some objects having metallicities below a tenth Solar, below that inferred for our sample or for the high redshift population at $z \sim 5$. Thus, while both our sample and the BCD sample can be characterised as compact star-forming galaxies, it is likely that the BCD sample provides a better match for galaxy populations at still earlier times ($z > 8$), when both typical metallicity and typical luminosity are expected to be rather lower than at $z \sim 5$. None of our sample would be classified as BCDs.

The 'Green peas' or extreme emission line galaxies (EELGs) are a sample of local ($0.112 < z < 0.360$) SDSS galaxies with strong nebular emission lines, particularly the [O III] λ5007 Å line in the SDSS r-band giving rise to a green appearance (Cardamone et al. 2009; Amorín et al. 2015). However, there are significant differences between our sample and these extreme emission-line sources. While most of the Peas/EELGs are identified as star-forming, some objects fall on the AGN or 'composite' regions of the BPT diagram. Their selection technique also differs in important respects from the LBG selection. They are required to show strong optical nebular features, particularly the [O III] line, and no constraint is placed on the ultraviolet continuum. This is effectively a selection on emission line equivalent width, more akin to Lyman-α emitter (LAE) selection than typical Lyman-break selection techniques.

To demonstrate the complementarity of our LBA sample and the EELGs, it is interesting to consider the Hydrogen recombination line strengths. High redshift ($z \gtrsim 5$) galaxies are observed in the rest-frame ultraviolet and thus usually characterised by their Lyman-α emission line. Both the Pea/EELG sample and our own sample of LBAs are observed in the rest-frame optical and their properties therefore most easily quantified in the Balmer series. A comparison between the two is not entirely straightforward. Lyman-α is resonantly scattered and its radiative transfer can be complex. Nonetheless, we can infer a predicted rest-frame Lyman-α equivalent width from the Hα feature in the low redshift samples. To do so we use stellar population synthesis models to model the scaling from Hα equivalent width to Lyman-α at the typical age of each sample. We also adjust the inferred Lyman-α emission to recover the predicted emission in the presence of dust, assuming a typical extinction $E_{cont}(B-V) = 0.1$, and account for the higher extinction of the emission lines relative to the stellar continuum according to the prescription of Calzetti et al. (2000).

In figure 15, we consider the comparison between the Green Pea sample of Cardamone et al. (2009), the $z = 5$ sample of spectroscopically-confirmed Lyman break galaxies from Douglas et al. (2010) and the sample presented in this paper, based on hydrogen line equivalent width. While neither analogue sample fully reproduces the observed $z \sim 5$ distribution, it is notable that only 22±4 per cent of the Douglas et al. sample had a rest-frame equivalent width exceeding 20 Å - quite unlike the distribution seen in the EELG sample. A significant difference in equivalent width distribution is indicative of a discrepancy in stellar population between samples since this is sensitive to the ratio of instantaneous star formation rate and its longer term average.

Figure 15. The equivalent width distributions of Lyman-α in the $z \sim 5$ Lyman break galaxy sample of Douglas et al. (2010), in the Green Pea sample of Cardamone et al. (2009) and in our sample. In the latter two cases, a predicted Lyman-α equivalent width has been inferred from their Balmer line emission as discussed in section 7.2.

7.3 Future Work

The study of this sample of analogue galaxies is still at an early stage. These galaxies provide an ideal laboratory to characterise the expected behaviour of line ratios, metallicity indicators, gas densities, and temperatures which will be directly probed at high redshifts in the JWST/ELT era. Any discrepancy between their nebular properties and those measured directly at high-z may thus be attributed to large scale intergalactic and radiation field properties rather than the local intense starburst activity. Such physical processes may underlie the evolution of the mass-metallicity relation. Line emission analysis will also yield outflow speeds and geometry for our objects, and the kinematics of different emission lines can provide insights into the age of the outflows and accretion.

Measuring the sub-millimetre flux of this sample will allow us to directly probe the obscured star formation in them, as well as putting constraints on their dust mass, extinction and emission properties. Exploring the gas masses of our objects will complement such studies, enabling us to determine star formation efficiencies, and how the fraction of gas in the galaxies has changed over time. Davies et al. (2010) and others (e.g. Coppin et al. 2015) have determined the molecular gas content of $z \sim 5$ LBGs from CO line emission. Similar observations of our local analogue sample will yield better constraints on the H_2 mass, and possibly detection of CO lines not achievable even through stacking of high redshift images.

Finally, radio continuum and line observations of this sample will provide an independent measurement of dust-obscured star formation rate and, in combination with other SFR indicators, may be sensitive to the age of the stellar population. 21 cm line observations will directly probe their atomic gas content, while similar measurements at $z \sim 5$ will not be possible before the advent of the SKA.

8 SUMMARY AND CONCLUSIONS

In this paper we establish a population of galaxies which resembles $z \sim 5$ LBGs in their observed properties. Using colour cuts on SDSS and GALEX archival data to identify objects which would fulfill the drop-out criteria of LBGs, as

well as UV-optical slopes indicative of young stellar populations, we selected a sample of 180 $0.05 < z < 0.25$ galaxies. We performed SED fitting on this sample using Maraston (2005) and BPASS (Eldridge & Stanway 2009, 2012) stellar population synthesis codes. Our analysis of best-fitting models allowed us to determine the objects' best-fitting ages, masses, and dust content. In addition, we calculate star formation rates, metallicities, and excitation measurements. Both observed and inferred properties have been compared to those determined for different galaxy populations, including $z \sim 5$ LBGs.

Our main findings include the following:

(i) We determine a median stellar mass for our sample of $\log(M_*/M_\odot) \sim 9.80 \pm 0.42$, in agreement with the masses found for $z \sim 5$ LBGs. The median age of the sample is $\log(\text{age/yr}) = 8.60 \pm 0.52$, indicating that, if our sample was redshifted to $z \sim 5$, their formation redshifts would be $z \sim 6-7$. The $E_{\text{cont}}(B-V)$ values, found using the Calzetti et al. (2000) starburst extinction law, showed little to moderate dust reddening with a median of 0.12 ± 0.07.

(ii) Using observed flux measurements as well as spectroscopic data, we determine median star formation rates between ~ 2.5 and 14 $M_\odot$ yr^{-1}, depending on SFR indicator, and mean specific star formation rates of $\sim 10^{-9}$ yr^{-1}.

(iii) Comparing these properties to those of $z \sim 5$ LBGs in table 1, we find good agreement. We therefore conclude that our sample can be used, with caution, as a local analogue population.

ACKNOWLEDGEMENTS

SMLG is funded by a research studentship from the UK Science and Technology Facilities Council (STFC). ERS also acknowledges support from STFC consolidated grant ST/L000733/1 and from the University of Warwick's Research Development Fund.

This paper has made use of data from the Sloan Digital Sky Survey (SDSS). The Sloan Digital Sky Survey (SDSS) is a joint project of The University of Chicago, Fermilab, the Institute for Advanced Study, the Japan Participation Group, The Johns Hopkins University, the Los Alamos National Laboratory, the Max-Planck-Institute for Astronomy (MPIA), the Max-Planck-Institute for Astrophysics (MPA), New Mexico State University, University of Pittsburgh, Princeton University, the United States Naval Observatory, and the University of Washington. Funding for the project has been provided by the Alfred P. Sloan Foundation, the Participating Institutions, the National Aeronautics and Space Administration, the National Science Foundation, the U.S. Department of Energy, the Japanese Monbukagakusho, and the Max Planck Society. www.sdss.org is a winner of the Griffith Observatory's Star Award.

This publication makes use of data products from the Two Micron All Sky Survey, which is a joint project of the University of Massachusetts and the Infrared Processing and Analysis Center/California Institute of Technology, funded by the National Aeronautics and Space Administration and the National Science Foundation. This publication also makes use of data products from the Wide-field Infrared Survey Explorer, which is a joint project of the University of California, Los Angeles, and the Jet Propulsion Laboratory/California Institute of Technology, funded by the National Aeronautics and Space Administration.

We also make use of Ned Wright's very useful online cosmology calculator (Wright 2006) and the TOPCAT table operations software (Taylor 2005).

For data analysis, we make use of the IRAF software environmnet. IRAF is distributed by the National Optical Astronomy Observatory, which is operated by the Association of Universities for Research in Astronomy (AURA) under a cooperative agreement with the National Science Foundation.

REFERENCES

Abazajian K. N., et al., 2009, ApJS, 182, 543
Allen C. W., 1976, Astrophysical Quantities
Amorín R., et al., 2015, A&A, 578, A105
Baldwin J. A., Phillips M. M., Terlevich R., 1981, PASP, 93, 5
Boutsia K., et al., 2014, A&A, 563, A142
Bouwens R. J., Illingworth G. D., Franx M., Ford H., 2007, ApJ, 670, 928
Bouwens R. J., et al., 2015, ApJ, 803, 34
Brinchmann J., Charlot S., White S. D. M., Tremonti C., Kauffmann G., Heckman T., Brinkmann J., 2004, MNRAS, 351, 1151
Burgarella D., Buat V., Iglesias-Páramo J., 2005, MNRAS, 360, 1413
Bunker A. J., et al., 2010, MNRAS, 409, 855
Calzetti D., Armus L., Bohlin R. C., Kinney A. L., Koornneef J., Storchi-Bergmann T., 2000, ApJ, 533, 682
Cardamone C., et al., 2009, MNRAS, 399, 1191
Cluver M. E., et al., 2014, ApJ, 782, 90
Coppin K. E. K., et al., 2015, MNRAS, 446, 1293
Corbin M. R., Vacca W. D., Cid Fernandes R., Hibbard J. E., Somerville R. S., Windhorst R. A., 2006, ApJ, 651, 861
Dale D. A., Helou G., Magdis G. E., Armus L., Díaz-Santos T., Shi Y., 2014, ApJ, 784, 83
Damen M., Labbé I., Franx M., van Dokkum P. G., Taylor E. N., Gawiser E. J., 2009, ApJ, 690, 937
Davies L. J. M., Bremer M. N., Stanway E. R., Birkinshaw M., Lehnert M. D., 2010, MNRAS, 408, L31
Davies L. J. M., et al., 2015, MNRAS, 452, 616
Dayal P., Ferrara A., Dunlop J. S., Pacucci F., 2014, MNRAS, 445, 2545
Dopita M. A., Kewley L. J., Sutherland R. S., Nicholls D. C., 2016, Ap&SS, 361, #61
Douglas L. S., Bremer M. N., Stanway E. R., Lehnert M. D., 2007, MNRAS, 376, 1393
Douglas L. S., Bremer M. N., Lehnert M. D., Stanway E. R., Milvang-Jensen B., 2010, MNRAS, 409, 1155
Driver S. P., et al., 2011, MNRAS, 413, 971
Eldridge J. J., Stanway E. R., 2009, MNRAS, 400, 1019
Eldridge J. J., Stanway E. R., 2012, MNRAS, 419, 479
Ellis R. S., et al., 2013, ApJ, 763, L7
Ferland G. J., Korista K. T., Verner D. A., Ferguson J. W., Kingdon J. B., Verner E. M., 1998, PASP, 110, 761
Finkelstein S. L., Rhoads J. E., Malhotra S., Grogin N., 2009, ApJ, 691, 465
Finkelstein S. L., et al., 2015, ApJ, 810, 71
Gonçalves T. S., et al., 2010, ApJ, 724, 1373
González V., Labbé I., Bouwens R. J., Illingworth G., Franx M., Kriek M., Brammer G. B., 2010, ApJ, 713, 115
González V., Bouwens R. J., Labbé I., Illingworth G., Oesch P., Franx M., Magee D., 2012, ApJ, 755, 148

Haberzettl L., Williger G., Lehnert M. D., Nesvadba N., Davies L., 2012, ApJ, 745, 96
Harford A. G., Gnedin N. Y., 2003, ApJ, 597, 74
Hathi N. P., et al., 2013, ApJ, 765, 88
Heckman T. M., et al., 2005, ApJ, 619, L35
Heckman T. M., et al., 2011, ApJ, 730, 5
Hoopes C. G., et al., 2007, ApJS, 173, 441
Hopkins A. M., et al., 2003, ApJ, 599, 971
Huang K.-H., et al., 2015, preprint, (arXiv:1504.02099)
Juneau S., Dickinson M., Alexander D. M., Salim S., 2011, ApJ, 736, 104
Kauffmann G., et al., 2003, MNRAS, 346, 1055
Kennicutt Jr. R. C., 1998, ARA&A, 36, 189
Kewley L. J., Dopita M. A., Sutherland R. S., Heisler C. A., Trevena J., 2001, ApJ, 556, 121
Kewley L. J., Geller M. J., Jansen R. A., 2004, AJ, 127, 2002
Lee J. C., Hwang H. S., Ko J., 2013, ApJ, 774, 62
Lehnert M. D., Bremer M., Verma A., Douglas L., Forster Schreiber N., 2007, preprint, (arXiv:0708.3000)
Leslie S. K., Kewley L. J., Sanders D. B., Lee N., 2016, MNRAS, 455, L82
Liske J., et al., 2015, MNRAS, 452, 2087
Ly C., Malkan M. A., Hayashi M., Motohara K., Kashikawa N., Shimasaku K., Nagao T., Grady C., 2011, ApJ, 735, 91
Madau P., Pozzetti L., Dickinson M., 1998, ApJ, 498, 106
Maraston C., 2005, MNRAS, 362, 799
Martin D. C., et al., 2005, ApJ, 619, L1
Mosleh M., et al., 2012, ApJ, 756, L12
Nandra K., Laird E. S., Steidel C. C., 2005, MNRAS, 360, L39
Noeske K. G., et al., 2007, ApJ, 660, L47
Oesch P. A., et al., 2013, ApJ, 772, 136
Oteo I., et al., 2013, MNRAS, 435, 158
Papovich C., Dickinson M., Ferguson H. C., 2001, ApJ, 559, 620
Rafelski M., Wolfe A. M., Cooke J., Chen H.-W., Armandroff T. E., Wirth G. D., 2009, ApJ, 703, 2033
Reddy N. A., Pettini M., Steidel C. C., Shapley A. E., Erb D. K., Law D. R., 2012, ApJ, 754, 25
Rhoads J. E., et al., 2013, ApJ, 773, 32
Roehlly Y., Burgarella D., Buat V., Boquien M., Ciesla L., Heinis S., 2014, ASPC, 485, 347
Scarlata C., et al., 2009, ApJ, 704, L98
Schlafly E. F., Finkbeiner D. P., 2011, ApJ, 737, 103
Shapley A. E., Steidel C. C., Adelberger K. L., Dickinson M., Giavalisco M., Pettini M., 2001, ApJ, 562, 95
Skrutskie M. F., et al., 2006, AJ, 131, 1163
Smith J. D. T., et al., 2007, ApJ, 656, 770
Stanway E. R., Davies L. J. M., 2014, MNRAS, 439, 2474
Stanway E. R., Eldridge J. J., Greis S. M. L., Davies L. J. M., Wilkins S. M., Bremer M. N., 2014, MNRAS, 444, 3466
Steidel C. C., Giavalisco M., Pettini M., Dickinson M., Adelberger K. L., 1996, ApJ, 462, L17
Steidel C. C., et al., 2014, ApJ, 795, 165
Taylor M. B., 2005, ASPC, 347, 29
Verma A., Lehnert M. D., Förster Schreiber N. M., Bremer M. N., Douglas L., 2007, MNRAS, 377, 1024
Wilkins S. M., Bunker A. J., Stanway E., Lorenzoni S., Caruana J., 2011, MNRAS, 417, 717
Wright E. L., 2006, PASP, 118, 1711
Wright E. L., et al., 2010, AJ, 140, 1868
Yabe K., Ohta K., Iwata I., Sawicki M., Tamura N., Akiyama M., Aoki K., 2009, ApJ, 693, 507
Zhao Y., Gu Q., Gao Y., 2011, AJ, 141, 68
Zwicky F., 1965, ApJ, 142, 1293
da Cunha E., Charlot S., Elbaz D., 2008, MNRAS, 388, 1595
van der Burg R. F. J., Hildebrandt H., Erben T., 2010, A&A, 523, A74

This paper has been typeset from a TEX/LATEX file prepared by the author.

Sample	redshift	mass (median)	dust extinction	age	SFR	sSFR	metallicity
		$\log_{10}(M_\odot)$	$E_{\rm cont}(B-V)$	$\log_{10}$(yrs)	$M_\odot$ yr^{-1}	log(yr^{-1})	$Z_\odot$
Our Sample	0.05 - 0.25	9.80 ± 0.42	$\sim 0.12 \pm 0.07$	$\sim 8.1 - 9.0$	~ 14 (UV)	$\sim -9.0 \pm 0.5$	~ 0.5
$z \sim 5$ LBGs[a]	~ 5	$8 - 11$ (~ 9)	~ 0.2	< 8	$\sim$ few 10s	~ -8.7[e]	~ 0.2
LBAs[b] to $z \sim 3$	$0 < z < 0.3$	$\sim$ 9.0 to 10.9	$A_{FUV} \sim 0 - 2$mag	~ 9 (doubling time)	few 10s - 100s	-9.8 to -8	$0 \sim 0.3 - 1.5$
Green Peas[c]	$0.112 < z < 0.360$	8.5 - 10	$\leqslant 0.25$	~ 8 (doubling time)	~ 10	up to -8	~ 1
Blue Compact Dwarfs[d]	$z < 0.01$	7-8	low	$\sim$6-10[f]	$\sim 10^{-3} - 1$	-	$\sim \frac{1}{10}$

Table 1. a =Verma et al. (2007); Douglas et al. (2010); Yabe et al. (2009) from; b = from Heckman et al. (2005), Hoopes et al. (2007), Gonçalves et al. (2010); solar metallicity is taken as log[O/H] +12 $\sim$ 8.7; c = Cardamone et al. (2009), d = Corbin et al. (2006), Zhao et al. (2011); e=González et al. (2010); f = the younger (1-10 Myr) population dominates the light while older (10 Gyr) stars dominate the mass